

# Magnetospheric flux transport in the Dungey cycle during 2010

S. E. Milan<sup>1,2\*</sup>, J. A. Carter<sup>1</sup>, H. Sangha<sup>1</sup>, G. Bower<sup>1</sup>, and B. J. Anderson<sup>3</sup>

<sup>1</sup>Department of Physics and Astronomy, University of Leicester, Leicester, UK.

<sup>2</sup>Birkeland Centre for Space Sciences, University of Bergen, Norway.

<sup>3</sup>Johns Hopkins University Applied Physics Laboratory, Laurel, Maryland, USA.

## Key Points:

- We determine convection state and magnetic flux transport continuously for the duration of 2010
- Most magnetic flux transport occurs during substorm growth and driven phases (when day and nightside reconnection balance)
- We provide a framework for understanding isolated substorms and substorms occurring during prolonged convection activity

---

\*Department of Physics and Astronomy, University of Leicester, Leicester LE1 7RH, UK

Corresponding author: Steve Milan, [steve.milan@le.ac.uk](mailto:steve.milan@le.ac.uk)

## Abstract

We quantify the contributions of different convection states to the magnetic flux throughput of the magnetosphere during 2010. To do this we provide a continuous classification of convection state for the duration of 2010 based upon observations of the solar wind and interplanetary magnetic field, geomagnetic indices, and field-aligned currents measured by the Active Magnetosphere and Planetary Electrodynamics Response Experiment (AMPERE). Convection states are defined as 1) quiet and 2) weak activity, substorm 3) growth, 4) expansion, and 5) recovery phases, 6) substorm driven phase (when relatively steady magnetospheric convection occurs), 7) recovery bays (when recovery phase is accompanied by a negative excursion of the AL electrojet index), and 8) periods of multiple intensifications (storm-time periods when continuous short-period AL activity occur). The magnetosphere is quiet for 46% of the time, when very little convection takes place. The majority of convection occurs during growth and driven phases (21% and 38%, respectively, of open magnetic flux accumulation by dayside reconnection). We discuss these results in the context of the expanding/contracting polar cap model of convection, and describe a framework within which isolated substorms and disturbances during periods of more continuous solar wind-magnetosphere driving can be understood.

## Plain Language Summary

Space weather within the Earth’s geospace environment, including vivid auroral displays and geomagnetic activity that is damaging for satellites, telecommunications, global positioning systems, power distribution and pipelines, is caused by the interaction between the solar wind and the terrestrial magnetic field. We use observations of the solar wind, electric currents in the magnetosphere, and magnetic perturbations on the ground to analyse geomagnetic activity continuously for the whole of 2010. This allows us to determine that a range of responses are excited in the magnetosphere by different solar wind conditions, and to quantify the solar wind conditions that lead to most activity.

## 1 Introduction

In this study we provide a continuous classification of magnetospheric convection state for the duration of 2010 to quantify the overall contributions of different states to the magnetic flux throughput of the system. Such activity is driven by magnetic reconnection at the dayside magnetopause, interlinking the Earth’s magnetic field with the interplanetary magnetic field (IMF) carried by the solar wind, and the subsequent release of the IMF by reconnection in the magnetotail, together exciting the Dungey cycle of convection (Dungey, 1961). Variability of the dayside reconnection rate leads to a variety of time-dependent responses of the magnetosphere, most notably substorms and periods of steady magnetospheric convection, which can be described by the expanding/contracting polar cap model or ECPC (Cowley & Lockwood, 1992; Lockwood & Cowley, 1992; Milan, 2015). The ECPC has been employed to investigate the response of the magnetosphere to solar wind driving, either as case studies of a limited number of events (e.g., Milan et al., 2003, 2007, 2008; Milan, 2004; Hubert et al., 2006, 2017), or as statistics of many events (e.g., Milan, Grocott, et al., 2009; Milan, Hutchinson, et al., 2009; Clausen et al., 2013; Coxon et al., 2014; Walach & Milan, 2015; Milan et al., 2019). A drawback of such studies has been that they tend to focus on “interesting” periods rather a longitudinal analysis of geomagnetic activity (or lack thereof) over a prolonged period of time. To our knowledge, only Lockwood et al. (2009) have previously attempted a continuous breakdown of activity over an extended interval (the duration of 2001).

Previous workers have compiled lists of substorm onsets (e.g., Frey et al., 2004; Newell & Gjerloev, 2011; Forsyth et al., 2015) or periods of steady magnetospheric convection (e.g., Kissinger et al., 2011) using, for instance, magnetometer measurements (usually

the AU/AL electrojet indices) or global auroral imagery. These provide a useful framework for interpreting other geophysical observations. However, they tend to be based on a single observable that can be misinterpreted in isolation (e.g., Walach & Milan, 2015). In addition, “onset lists” do not provide information on the magnetospheric behaviour between onsets. In this study we employ a variety of solar wind and magnetospheric indicators with the aim of (a) reducing ambiguity in the determination of convection state and (b) providing an unbroken record of convection state over a prolonged period of time.

The rate of change of open (polar cap) flux,  $F_{PC}$ , is determined by the competition between the dayside (magnetopause) reconnection rate,  $\Phi_D$ , and the nightside (magnetotail) reconnection rate,  $\Phi_N$ ,

$$\frac{dF_{PC}}{dt} = \Phi_D - \Phi_N, \quad (1)$$

(Siscoe & Huang, 1985; Cowley & Lockwood, 1992; Milan et al., 2015).  $\Phi_D$  is the rate at which magnetospheric flux is opened, usually assumed to occur at the low latitude magnetopause; it does not include high latitude lobe reconnection as this produces no net opening of flux. Reconnection in the magnetotail can occur either at a distant neutral line (DNL) or near-Earth neutral line (NENL) (Hones Jr., 1984; Baker et al., 1996).  $\Phi_N$  refers specifically to the reconnection site that is actively closing open lobe flux; although in principle both a DNL and NENL can be active simultaneously, only one contributes to  $\Phi_N$ . Consider a situation in which a NENL forms during a period when a pre-existing DNL is active and closing flux at a rate  $\Phi_N$ . Initially the NENL will reconnect closed flux to grow a plasmoid, but will not contribute to  $\Phi_N$ . If the NENL reconnection rate exceeds the DNL rate, then eventually the plasmoid will be pinched off, at which point the NENL will dictate  $\Phi_N$ , the DNL now sitting on disconnected field lines propagating down-tail with the plasmoid (see also discussion in Russell (2000)).

As  $F_{PC}$  increases or decreases with time, and the magnetotail correspondingly inflates or deflates, flows are excited in the magnetosphere and ionosphere to maintain the magnetopause in stress balance with the flow of the solar wind (Cowley & Lockwood, 1992). Convection is quantified as the rate of transport of magnetic flux by these flows through the magnetosphere and across the polar cap, known as the cross-polar cap potential or transpolar voltage,  $\Phi_{PC}$ . Assuming that the polar cap remains roughly circular as it expands and contracts,

$$\Phi_{PC} = (\Phi_D + \Phi_N)/2 \quad (2)$$

(Lockwood, 1991).  $F_{PC}$  is observed to remain within the range 0.2 to 1.2 GWb (Milan et al., 2007), implying that on timescales of several hours the average dayside and nightside reconnection rates must equal, such that

$$\langle \Phi_{PC} \rangle = \langle \Phi_D \rangle = \langle \Phi_N \rangle. \quad (3)$$

Convective flows are a major source of geomagnetic activity. Convection is associated with horizontal currents in the ionosphere, and convection shears produce field-aligned currents (FACs) that close the circuit between the ionosphere and magnetosphere. The dominant FACs are the region 1 and 2 (R1/R2) currents first described by Iijima and Potemra (1976, 1978), which are coincident with the convection reversal boundary and the equatorward boundary of the convection pattern, respectively. The locations of these FACs depend on the size of the polar cap, and hence can be used to estimate  $F_{PC}$ . Particle precipitation carrying FACs produces the main auroral oval and increases the ionospheric conductance, in turn modifying the horizontal currents. Convection and conductance variability, especially associated with substorms, produces the magnetic perturbations measured as geomagnetic activity by the upper and lower auroral electrojet indices, AU and AL (Davis & Sugiura, 1966). Convection also controls the injection of plasma into the inner magnetosphere and its energisation, leading to enhancements of

the ring current and storm-time magnetic perturbations measured by the SYM-H index (Iyemori, 1990).

The behaviour of the magnetosphere depends largely on the interplay between  $\Phi_D$  and  $\Phi_N$ . The dayside reconnection rate is directly and promptly controlled by conditions in the solar wind, including its speed and the magnitude and orientation of the embedded interplanetary magnetic field (IMF) (Milan et al., 2012, and references therein). The nightside reconnection rate is somewhat decoupled from the dayside rate, though must balance the dayside rate over periods of several hours, is described by eq. (3). As  $F_{PC}$  increases the magnetotail becomes inflated and the magnetopause flares outwards, intercepting the flow of the solar wind. The pressure exerted by the solar wind on the magnetopause is exerted through the magnetotail lobes and onto the plasma sheet, which thins, leading to conditions conducive to the onset of magnetotail reconnection (Slavin et al., 2002; Milan et al., 2006, 2008). It has also been speculated that the magnetic perturbation produced by an enhanced ring current can counteract this thinning and inhibit the onset of reconnection (Milan, Hutchinson, et al., 2009). Then, the onset of tail reconnection is a competition between these two influences.

The behaviour is usually described in terms of the growth, expansion, and recovery phases of the substorm cycle (McPherron, 1970; McPherron et al., 1973; Rostoker et al., 1980; Lockwood & Cowley, 1992). The growth phase follows a southward turning of the IMF,  $\Phi_D > 0$  and  $\Phi_N \approx 0$  such that  $dF_{PC}/dt > 0$ , the polar cap expands and the auroral oval progresses to lower latitudes. At some point reconnection is initiated in the magnetotail (see above),  $\Phi_N > 0$ , and intense auroras form the substorm auroral bulge, which tends to expand polewards as open flux is closed, known as the substorm expansion phase. The auroral bulge is associated with the formation of the substorm current wedge and westward substorm electrojet which produces a sharp negative excursion in the AL index – the substorm bay. A northward turning of the IMF then leads to substorm recovery phase, during which  $\Phi_D \approx 0$  but persistent magnetotail reconnection,  $\Phi_N > 0$ , leads to  $dF_{PC}/dt < 0$ , the polar cap contracts and the auroral oval progresses to higher latitudes. Eventually nightside reconnection switches off and the magnetosphere enters a quiescent state. Between the expansion and recovery phases, if the IMF remains southwards for a prolonged period, the nightside reconnection rate can settle such that  $\Phi_N \approx \Phi_D$  and  $dF_{PC}/dt \approx 0$  (Walach & Milan, 2015; Milan et al., 2019). Periods of  $\Phi_N \approx \Phi_D$  have been known as balanced reconnection intervals (BRIs) (DeJong et al., 2008), periods of steady magnetospheric convection (SMC) (Sergeev et al., 1996; McWilliams et al., 2008; Kissinger et al., 2012), convection bays (Sergeev et al., 2001), and steady convection events (SCE) (Lockwood et al., 2009). We now introduce the term driven phase to describe this aspect of the substorm cycle.

In Section 2 we describe the observables we use in this study and the convection states that we identify. Section 3 presents an analysis of the occurrence of different states and the sequences of states that represent substorms and other forms of geomagnetic activity. Finally, we conclude and describe future directions for research in Section 4.

## 2 Methodology

We determine magnetospheric convection state continuously for the duration of 2010. A few data gaps are present in the data, and the total period of analysis comprises just over 360 full days. Figure 1 shows a 60 h interval from May, which we discuss below. This interval is chosen as it is typical, but also contains examples of all the convection states discussed in this paper.

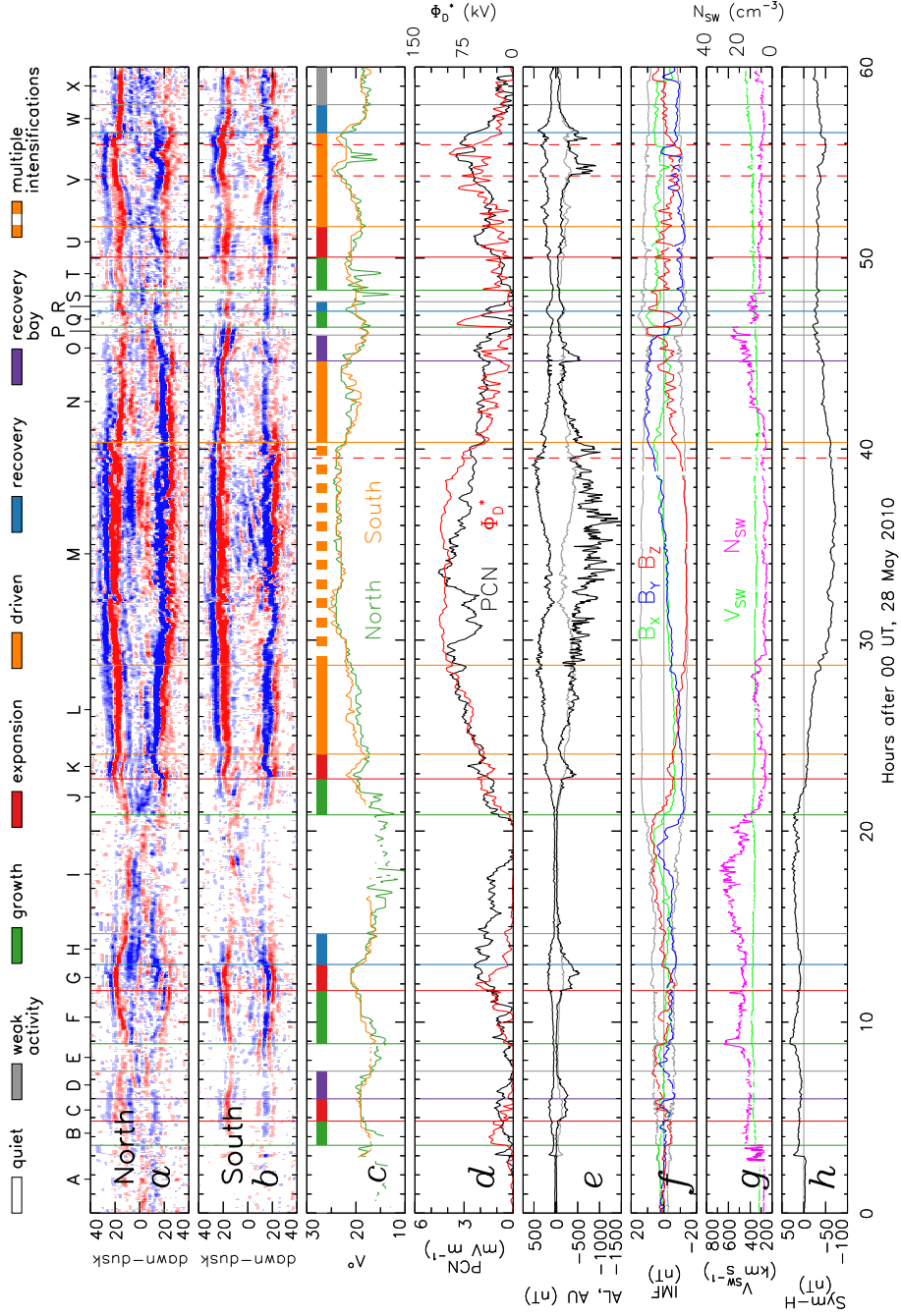


**Figure 1.** Observations and magnetospheric state classifications for a 60 h period following 00 UT, 28 May 2010. (a) and (b) Keograms of AMPERE field-aligned currents across the dawn-dusk meridian in the Northern and Southern Hemispheres. Red and blue represent upward and downward FACs, the colour scale saturating at  $\pm 0.5 \mu\text{A m}^{-2}$ . (c) The radius of a circle fitted to the boundary between R1 and R2 currents,  $\Lambda$ , in the two hemispheres, which is a proxy for polar cap flux  $F_{PC}$ . (d) The PCN geomagnetic index, a proxy for cross-polar cap potential  $\Phi_{PC}$ , and  $\Phi_D^*$ , a proxy for dayside reconnection rate. (e) AU and AL (black lines); -AU (grey line) for comparison with AL. (f) The  $B_X$ ,  $B_Y$ , and  $B_Z$  components of the IMF. (g) Solar wind speed,  $V_{SW}$ , and density,  $N_{SW}$ . (h) The SYM-H geomagnetic index.

## 2.1 Parameters

Our classification of convection state is based on a consideration of the auroral electrojet indices, AU and AL, dayside and nightside reconnection rates, polar cap open flux and the cross-polar cap potential.  $F_{PC}$ ,  $\Phi_D$ ,  $\Phi_N$ , and  $\Phi_{PC}$  are important parameters for understanding magnetospheric convection, though in general are difficult to measure accurately. As described below we use proxies,  $F_{PC}^*$ ,  $\Phi_D^*$ , and  $\Phi_{PC}^*$ , for three of these parameters;  $\Phi_N$  can be inferred from these using eqs. (1) and (2).

Additional parameters are included in the analysis, but are not used to determine the state classifications: the geomagnetic index SYM-H, the solar wind speed and density, and IMF magnitude and orientation. Geomagnetic indices and solar wind parameters are derived from the 1-min OMNI dataset (King & Papitashvili, 2005). We also use observations of FACs from the Advanced Magnetosphere and Planetary Electrodynamics Response Experiment (AMPERE) which uses magnetometer measurements from the Iridium telecommunications constellation to infer currents poleward of  $40^\circ$  geomagnetic latitude at a cadence of 2 min (see e.g., Anderson et al., 2000, 2002; Waters et al., 2001; Coxon et al., 2018).

### 2.1.1 FAC radius, $\Lambda$ , and polar cap flux, $F_{PC}^*$

Monitoring the polar cap or open magnetic flux is important for interpreting magnetospheric dynamics in the context of the ECPC model. Previous studies that have used global auroral imagery to estimate  $F_{PC}$  have faced the limitation that gaps in observation occur every orbit (e.g., Milan et al., 2007; Milan, Hutchinson, et al., 2009; Milan, 2009). AMPERE, on the other hand, provides continuous observations of the FACs in both hemispheres, with few breaks in continuity.

Panels (a) and (b) of Fig. 1 show keograms of AMPERE FACs along the dawn-dusk meridian of the Northern and Southern Hemispheres. The up/down pairs of R1 and R2 currents can be seen at both dawn and dusk, varying in magnitude with the strength of convection and moving in colatitude as the polar cap expands and contracts (Clausen et al., 2012; Milan, 2013; Milan et al., 2017, 2019). We use the radius of a circle fitted to the boundary between R1 and R2 FACs, determined using the method of Milan et al. (2015), as a proxy for  $F_{PC}$ . Fig. 1(c) shows this radius,  $\Lambda$ , determined independently from the FACs in both hemispheres.  $\Lambda$  can only be measured when the FACs are of sufficient magnitude that the boundary between R1 and R2 is readily identifiable. This occurs frequently in the summer hemisphere where the ionospheric conductance is high, and in the winter hemisphere when convection is active. The measurements from the two hemispheres are combined to provide a single estimate of  $\Lambda$ .

Burrell et al. (2020) confirmed that  $\Lambda$  is related to the location of the OCB, using DMSP spacecraft particle measurements. Figure 2(a) shows the relationship between  $\Lambda$  and our proxy  $F_{PC}^*$ , assuming that the polar cap boundary lies  $\Delta\Lambda = 3^\circ$  or  $4^\circ$  poleward of the R1/R2 boundary.  $F_{PC}^*$  is calculated as the radial component of a dipole field integrated over the polar regions within a circle of radius  $\Lambda - \Delta\Lambda$ , centred on a point displaced from the geomagnetic pole by  $4^\circ$  along the midnight meridian, the typical centre of the auroral oval and the R1/R2 FAC rings (this curve is insensitive to the choice of pole offset in the range  $0^\circ$  to  $10^\circ$ ). Assuming  $\Delta\Lambda = 4^\circ$ , a convenient relation between  $\Lambda^\circ$  and  $F_{PC}^*$  (GWb) over the range shown is

$$F_{PC}^* \approx 0.00182 \Lambda^2 - 0.009 \Lambda - 0.02, \quad (4)$$

indicated by the red line in Fig. 2(a). Figs. 2(b) and (c) show the occurrence and cumulative occurrence distributions of  $\Lambda$  in 2010; the median value is close to  $17.5^\circ$ , corresponding to  $F_{PC}^* \approx 0.4$  GWb, which is close to previous estimates of the typical polar cap size, made using different observational techniques (e.g., Milan et al., 2007; Boakes et al., 2008).

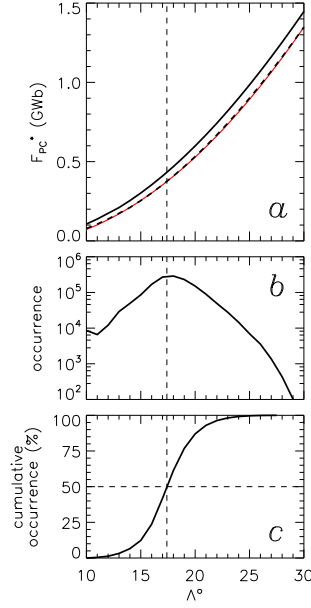


**Figure 2.** (a) Relationship between  $\Lambda$  and  $F_{PC}^*$  assuming that the polar cap boundary is circular and located  $3^\circ$  (full line) or  $4^\circ$  (dashed line) poleward of the boundary between R1 and R2 FACs. The red line shows eq. (4). (b) The occurrence distribution of  $\Lambda$  measured during 2010. (c) The associated cumulative occurrence distribution, showing that the median  $\Lambda \approx 17.5^\circ$ , or the median  $F_{PC}^* \approx 0.4$  GWb.

As will be discussed below,  $F_{PC}^*$  overestimates the true value of  $F_{PC}$  when a significant auroral bulge is present, as the assumption of the circularity of the polar cap breaks down (Mooney et al., 2020).

### 2.1.2 Dayside reconnection rate, $\Phi_D^*$

The low latitude magnetopause reconnection rate is predicted from the upstream solar wind speed and (GSM) interplanetary magnetic field components using the parameterisation of Milan et al. (2012):

$$\Phi_D^* = 3.2 \times 10^5 V_{SW}^{4/3} B_{YZ} \sin^{9/2} \left| \frac{\theta}{2} \right|, \quad (5)$$

where  $\theta = \tan^{-1}(B_Y, B_Z)$  is the IMF clock angle and  $B_{YZ}^2 = B_Y^2 + B_Z^2$ .

Figure 3 tests the relationship between  $\Phi_D^*$  and  $F_{PC}^*$  expected from eq. (1), using data from 23 October 2010. Panel (a) shows  $\Lambda$  determined from AMPERE at 2 min cadence (grey curve), and with a Savitsky-Golay filter (11 point window, degree 3 polynomial) applied to provide smoothing (black curve). Repeated increases and decreases in  $\Lambda$  indicate substorm cycles (Milan et al., 2007; Clausen et al., 2012). In panel (d)  $\Lambda$  has been converted to  $F_{PC}^*$  using eq. (4). Panel (c) shows  $\Phi_D^*$  evaluated at 2 min cadence. Multiple data gaps in  $V_{SW}$  create gaps in  $\Phi_D^*$ , and where these are less than 10 min in duration we have linearly interpolated over the missing values.

Superimposed on panel (d) are curves of  $\int \Phi_D^* dt$  (red dashes), which predict from eq. (1) how  $F_{PC}$  should grow with time, assuming that  $\Phi_N = 0$ . Each of these curves is the same, but each has been vertically offset to match the variation in  $F_{PC}^*$ , blue circles indicating the points at which the matching has been performed. Vertical green and red lines indicate the starts of growth and expansion phases identified in the data (see



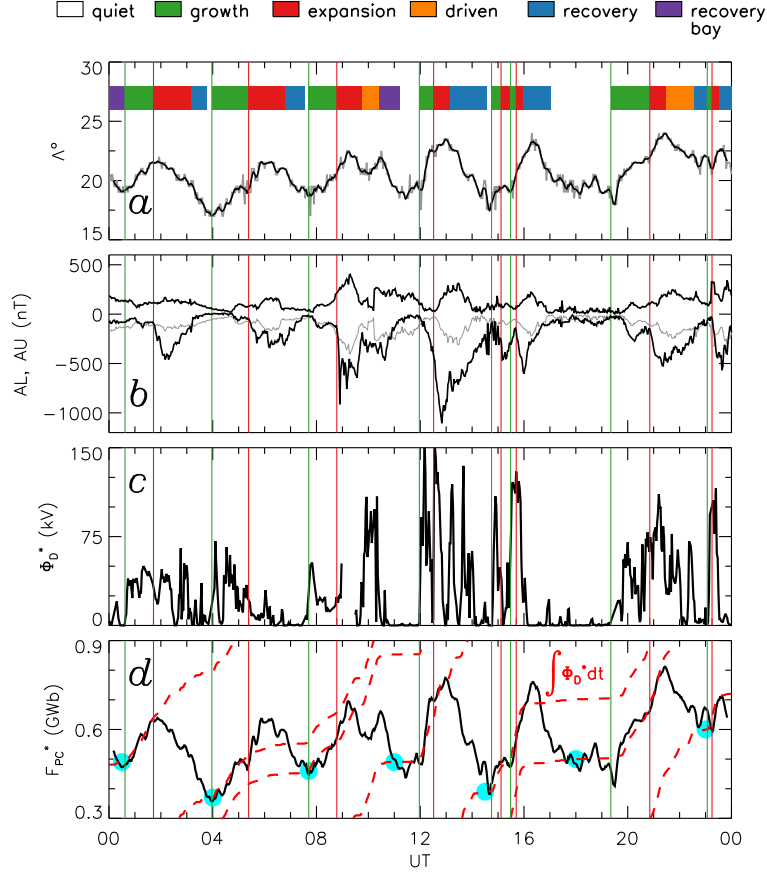


**Figure 3.** A comparison of polar cap size and dayside reconnection rate from 23 October 2010. (a) Radius of the R1/R2 field-aligned current boundary,  $\Lambda$ , measured by AMPERE (grey) and smoothed with a Savitsky-Golay filter (black). Convection state is indicated by coloured bars; green and red vertical lines indicate the start of growth and expansion phases. (b) AU and AL electrojet indices. (c) Dayside reconnection rate estimated from OMNI solar wind observations,  $\Phi_D^*$ . (d) Polar cap flux estimated from  $\Lambda$ ,  $F_{PC}^*$ . Superimposed are multiple copies of the curve  $\int \Phi_D^* dt$ , vertically offset to align with  $F_{PC}^*$  during growth phases; blue circles indicate where the curves have been matched up.



below); AU and AL are presented in panel (b) for reference. It is found that the growth in  $F_{PC}^*$  and  $\int \Phi_D^* dt$  match reasonably well during growth phases, giving confidence in our use of these proxies.

The vertical offset between subsequent  $\int \Phi_D^* dt$  curves indicates the amount of flux that has been closed in the intervening activity of each substorm, that is  $\int \Phi_N dt$ . In principle,  $\Phi_N$  can be estimated from these observations (Hubert et al., 2006; Milan et al., 2007), but we have not done this in the present study.

### 2.1.3 Polar cap index, PCN, and cross-polar cap potential, $\Phi_{PC}^*$

The polar cap index PCN measures the magnetic perturbation produced on the ground in the central (northern) polar cap produced by horizontal ionospheric currents associated with convection overhead (Troshichev et al., 2006). The index is scaled to closely match the magnitude of the solar wind geoeffective interplanetary electric field  $E_{KL}$  (the Kan-Lee coupling function (Kan & Lee, 1979)) and so is measured in units of  $\text{mV m}^{-1}$ . PCN is usually interpreted as solar wind energy input into the magnetosphere (Troshichev et al., 1979). However, the ionospheric flow to which the index is sensitive is the anti-sunward convection of the Dungey cycle, excited by the combined contributions of day-side and nightside reconnection, and as a consequence we use PCN as a proxy for the cross-polar cap potential,  $\Phi_{PC}$ .

The transport of magnetic flux within the magnetosphere leads to ionospheric convection during growth, expansion, driven, and recovery phases. From eq. 2 we expect the cross-polar cap potential during each substorm phase to be: growth,  $\Phi_{PC} \approx \Phi_D/2$ ; expansion,  $\Phi_{PC} \approx (\Phi_D + \Phi_N)/2$ ; driven,  $\Phi_{PC} \approx \Phi_D \approx \Phi_N$ ; recovery,  $\Phi_{PC} \approx \Phi_N/2$ . During quiescent periods we expect  $\Phi_{PC} \approx \Phi_D \approx \Phi_N \approx 0$ . Hence, we expect that during the typical growth-expansion-recovery phase sequence of a substorm  $\Phi_{PC}$  will be a smoothed version of  $\Phi_D$ , with a time lag of the order of the duration of the growth and recovery phases (Milan, 2004). A lagged cross-correlation between  $\Phi_D^*$  (kV) and PCN ( $\text{mV m}^{-1}$ ) indicates that  $\text{PCN} \approx \Phi_D^*/17$ , with a maximum correlation at a lag of approximately 30 mins (this can be confirmed by comparing variations in PCN and  $\Phi_D^*$  in Fig. 1(d)). Our proxy for the cross-polar cap potential is then  $\Phi_{PC}^* (\text{kV}) \approx 17 \text{ PCN}$ .

We note that during strong northward IMF conditions PCN can respond to polar cap flows driven by lobe reconnection, rather than being associated with the antisunward flow of the Dungey cycle, and is then not a good proxy for  $\Phi_{PC}$ .

### 2.1.4 Electrojet indices, AU and AL

AU and AL represent the maximum positive and negative northward magnetic perturbations measured at ground magnetometers located at auroral latitudes (Davis & Sugiura, 1966). During non-substorm periods these represent the strength of the eastward and westward auroral electrojets, related to the strength of convection in the Dungey cycle return flow regions, and it is expected that  $|\text{AL}| \approx \text{AU}$ . During substorm expansion phase the presence of the westward substorm electrojet introduces a negative perturbation to the AL index, in which case  $|\text{AL}| > \text{AU}$ ; such a “negative bay” in AL is commonly used as an indicator of substorm onset (e.g., Newell & Gjerloev, 2011; Forsyth et al., 2015). These two aspects, convection and substorm contributions to AU and AL, have been described as the “two component auroral electrojets” by Kamide and Kokubun (1996).

### 2.1.5 Ring current index, SYM-H

SYM-H is the north-south magnetic perturbation produced by the westward ring current measured at low latitude ground magnetometers (Iyemori, 1990). It is also affected by the magnetopause current, which produces a positive perturbation in SYM-

H when the solar wind ram pressure is high. It has been suggested that the magnetic perturbation produced by the ring current in the magnetotail can modulate the occurrence of tail reconnection (Milan, Hutchinson, et al., 2009).

## 2.2 Magnetospheric convection state categories

We subdivide 2010 into the following convection states: quiet, weak activity, sub-storm growth, expansion, driven, and recovery phases, recovery bays, and multiple intensifications; this dataset is available as Milan (2020). This categorisation is in the same spirit as that of Lockwood et al. (2009), though as our observations are available at higher temporal cadence, and many of our observables are different, we have adapted our definitions and added some additional states. These classifications are shown in Fig. 1(c) and by vertical lines in other panels; intervals have been labelled A to X to aid discussion. In the following sections we explain how we identified these states. We note that Lockwood et al. (2009) lamented that there was no “agreed standard set of definitions [of states] which would allow comparison with other studies,” and unfortunately this is still the case.

### 2.2.1 Quiescent

Periods of low dayside reconnection and no appreciable nightside activity,  $\Phi_D^* < 5$  kV,  $\Phi_N \approx \Phi_{PC}^* \approx 0$  are designated as *quiet* (A, E, I, P, S). Typically, the FAC currents are so weak that the R1/R2 pattern is unclear and  $\Lambda$  cannot be determined. During periods of strongly northward IMF, PCN may be elevated due to the occurrence of lobe reconnection, and is then not a good proxy for  $\Phi_{PC}^*$  (as seen during interval I).

### 2.2.2 Growth phase

*Growth phases* (B, F, Q, and T) begin with a southward turning of the IMF, or an increase of dayside coupling to  $\Phi_D^* > 10$  kV, leading to a progressive increase in  $\Lambda$ . AU and AL may become elevated, though  $|\text{AL}| \approx \text{AU}$ , indicating that there is no significant nightside activity,  $\Phi_N \approx 0$ . PCN can increase due to the driving of convection by dayside reconnection.

### 2.2.3 Expansion phase

Onset of the *expansion phase* (C, G, U) is typically marked by a negative excursion of AL (a *substorm bay*) such that  $|\text{AL}| > \text{AU}$ . In many cases  $\Lambda$  continues to increase for approximately 20 mins following expansion phase onset, but then levels off or decreases slightly indicating the onset of magnetotail reconnection with  $\Phi_N \approx \Phi_D$ .

### 2.2.4 Recovery phase

The start of the *recovery phase* (H, R) is marked by a northward turning of the IMF or a decrease in dayside driving to  $\Phi_D^* < 5$  kV.  $\Lambda$  usually decreases markedly during the recovery phase due to ongoing nightside reconnection,  $\Phi_N > \Phi_D$ . AU, AL, and PCN tend to decrease over the course of a recovery phase. The end of the recovery phase is usually a gradual transition to quiet conditions.

### 2.2.5 Driven phase

Often, the magnetosphere does not transition directly from expansion to recovery phase, but enters a period when dayside and nightside reconnection are approximately balanced, which we term *driven phases* (L, N, V). This occurs if the IMF remains southwards and  $\Phi_D^* > 10$  kV following the initial substorm bay in AL. This period may last

for a few 10s of minutes or many hours, depending on the variability of the IMF. During these periods,  $\Lambda$ , PCN, AU and AL remain approximately constant. Typically,  $|\text{AL}| \approx \text{AU}$ , though AL may also show negative excursions.

Lockwood et al. (2009) referred to such phases as steady convection events (SCEs) and likened them to periods of steady magnetospheric convection (SMC). In previous studies, periods of SMC are usually identified as having very steady AL over a minimum duration of several hours. In this study, we allow AL to vary somewhat, that is to encompass periods when intensifications in nightside reconnection may be ongoing. DeJong (2014) studied periods of SMC with steady and non-steady AL and concluded that these represent periods of weaker and stronger solar wind driving.

During driven phases  $\Phi_D \approx \Phi_N$  and  $F_{PC}$  is relatively constant, such that they have been referred to as balanced reconnection intervals (DeJong et al., 2008). However, there is no direct constraint on  $\Phi_N$  that it exactly equals  $\Phi_D$ , and slow changes in  $\Phi_D$  can result in a mismatch between the two, leading to gradual variations in  $F_{PC}$ ; we term this *quasi-balanced reconnection*. Occasionally, a gradual expansion in the polar cap during a driven phase can lead to an onset-like AL bay and a subsequent decrease in  $\Lambda$ . We note the time of these *driven phase onsets* for later analysis (though they are not considered to be a state category in themselves). Three such events have been represented as red vertical dashed lines during intervals M and V.

### 2.2.6 Multiple intensifications

Some driven phases during periods of strong solar wind coupling are characterised by large quasiperiodic negative excursions of AL, with a periods of 30-60 min. It is unclear if these represent individual substorms or are intensifications of the on-going nightside reconnection. The period of these intensifications is sufficiently short that no coherent expanding/contracting behaviour is seen in  $\Lambda$ , which remains relatively constant. We identify these as intervals of *multiple intensifications* (M). Such periods, when rapid changes in magnetic perturbations are observed on the ground, are those most likely to give rise to damaging space weather effects on ground-based infrastructure.

### 2.2.7 Recovery bays

Occasionally, the recovery phase at the end of a driven phase can be accompanied by an AL bay. Sergeev et al. (1996) noted that many SMC begin and end with a substorm, and Milan et al. (2019) noted that a substorm-like signature could accompany a northward turning of the IMF at the end of a period of SMC. We identify these periods as *recovery bays* (D, O).

### 2.2.8 Weak activity

During periods of relatively weak solar wind driving,  $\Phi_D^* < 10$  kV, AU, AL and PCN can be slightly elevated,  $\text{AU} \approx -\text{AL} \approx 50$  nT. However, no other coherent features are seen that identify the periods as growth, expansion, driven, or recovery phases. Also, often the R1/R2 FACs are too weak for  $\Lambda$  to be measured reliably. We refer to these as periods of *weak activity* (X).

## 3 Results and discussion

In the 360 full days of data that are included in the analysis, just under 3500 category boundaries and 196 driven phase onsets are identified. This dataset is available as Milan (2020). First we discuss the characteristics of each category, and then sequences of categories.

**Table 1.** Number and duration of each convection state category

Category	Number	Duration		
		Total (h)	Total (%)	Event (h)
Quiescent	799	3971.6	46.0	4.97
Weak activity	234	735.4	8.5	3.14
Growth phase	752	976.3	11.3	1.30
Expansion	568	470.0	5.4	0.83
Driven	447	1582.4	18.3	3.54
Recovery	502	559.3	6.5	1.11
Recovery bay	176	227.5	2.6	1.29
Multiple intensifications	12	119.3	1.4	9.94

**Table 2.** Average parameters during convection state categories

Category	$\Phi_D^*$ (kV)	PCN (nT)	AU (nT)	AL (nT)	SYM-H (nT)	Total $\int \Phi_D^*$ (GWb)	$\int \Phi_D^*$ (%)	$\Delta F_{PC}$ (GWb)
Quiescent	3.2	0.2	18.3	-16.7	-4.6	43.3	13.3	0.057
Weak activity	7.7	0.5	31.8	-40.7	-7.3	20.3	6.0	0.087
Growth	20.1	0.7	44.4	-46.1	-7.1	70.7	20.8	0.094
Expansion	19.6	1.1	66.8	-179.9	-10.4	33.2	9.8	0.059
Driven	22.5	1.2	77.7	-151.9	-14.9	128.1	37.6	0.287
Recovery	5.6	0.8	64.3	-99.8	-13.9	11.3	3.3	0.023
Recovery bay	4.8	0.8	61.7	-143.1	-11.9	3.9	1.2	0.022
Multiple intensifications	63.7	2.5	214.7	-522.6	-50.5	27.4	8.0	2.279

### 3.1 Convection state statistics

Table 1 summarises the number of each category, the total duration in terms of hours and percentage of the whole year, and the average duration of each event. Table 2 summarises the characteristics of the events, including average  $\Phi_D^*$ , PCN, AU, AL, and SYM-H. Also shown is the total amount of open flux created by dayside reconnection during each category,  $\int \Phi_D^* dt$ , in terms of GWb and as a percentage over the year, and as event averages, which we refer to as  $\Delta F_{PC}$ .

Quiescent periods account for almost half of the year, corresponding to periods when IMF  $B_Z > 0$ . There were almost 800 quiet periods, with an average duration of 5 h, though this duration is very variable. Although we expect little dayside coupling during these events,  $\Phi_D^*$  is a non-negative number and 13% of the estimated open flux accumulated by the magnetosphere over the course of the year occurs in this 46% of the time, though at an average rate of only 3.2 kV. AL, AU, and SYM-H are low during these periods. Weak activity is driven by  $\Phi_D^* \approx 8$  kV for 9% of the time, with an average duration of 3.1 h, and accounts for 6% of the accumulated open flux over the year.

Growth, expansion, and driven phases have on average  $\Phi_D^* \approx 20$  kV, and last approximately 1 h. As expected, during growth phases  $|AL| \approx AU$ ;  $|AL| > AU$  during expansion and driven phases, by a factor of 2.5 and 2, respectively. 21% of the open flux of the magnetosphere is accumulated during growth phases, whereas expansion and driven phases account for 10% and 38% of the flux throughput, respectively. The magnetosphere is in a driven state for 18% of the time, expansion and recovery phases accounting for 6% each.

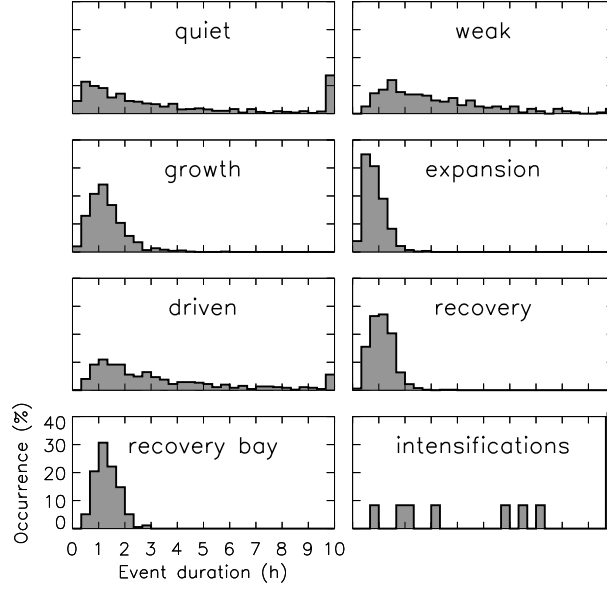


**Figure 4.** Distributions of event durations for each category, in bins of 20 min. The rightmost bin shows the number of events that exceed a duration of 10 h.

On average  $\Phi_D^* \approx 5$  kV during recovery and recovery bay phases. However, the flux closed by tail reconnection during these events must account for the flux opened during growth and expansion phases (assuming reconnection is approximately balanced during driven phases). The only parameter that apparently distinguishes between recovery phases with and without bays is the magnitude of AL.

The distribution of event duration for each category is presented in Figure 4. The distributions for growth, recovery, and recovery bay phases are all similar, peaking near 1 h (and median 1 h). This suggests that they represent the timescales over which magnetic flux is opened and closed prior to or following the establishment of a NENL. The expansion phase distribution is also similar, though peaks near 30 min (median 40 mins), and represents the timescale over which the magnetotail establishes this new NENL in response to open flux being accumulated in the magnetotail lobes. The quiet, weak, and driven phases also have distributions that resemble each other, though these are much broader (median 2 h). We interpret these as reflecting the variability of IMF  $B_Z$ , being the distributions of waiting times between significant north-south and south-north turnings of the IMF. Multiple intensifications have a distribution with a median of 5 h, presumably representing the timescale of intense storm periods.

The left panels of Figure 5 show distributions of IMF  $B_Y$  and  $B_Z$  for each category. In the main,  $\sqrt{B_Y^2 + B_Z^2} < 15$  nT in these distributions. All the distributions are approximately symmetric in IMF  $B_Y$ , though there was a slight tendency for  $B_Y < 0$  (and  $B_X > 0$ ) to dominate in 2010. The quiet distribution maximises for  $B_Z > 0$ , though short periods of  $B_Z < 0$  also occur owing to the high frequency variability of the solar wind. Weak activity periods are associated with  $B_Z \approx 0$ . Growth phases are predominantly associated with  $B_Z < 0$ , as expected, though there are also brief periods of  $B_Z > 0$  due to the variability of the solar wind. The expansion and driven phase distributions are the same as for growth phases. This indicates that growth, expansion, and driven phases are produced by the same solar wind driving conditions, and the demarcation into these different phases is due to the past activity within the magnetosphere and the natural evolution of substorms (e.g. growth to expansion to recovery). Recov-

ery and recovery bay phases both have distributions that resemble quiet phases (i.e. no or low solar wind driving).

The IMF  $B_X-B_Y$  distributions (not shown) for the different categories are in general consistent with a Parker spiral configuration ( $B_X \approx -B_Y$ ). Periods of multiple intensifications are unlike this, however, being dominated by a southward  $B_Z$  component, and an average  $\Phi_D^* > 60$  kV. These periods also have enhanced SYM-H with an average value of -50 nT. They only account for 1% of the year, but produce 8% of the open flux throughput of the magnetosphere.

The middle panels of Fig. 5 show the distributions of solar wind velocity and number density during each category. In 2010, the solar wind varied between periods of high solar wind speed and low solar wind density and periods of low speed and highly variable density (see also Section 3.4).  $V_{SW} \approx 450$  km s<sup>-1</sup> can be viewed as an approximate demarcation between the two types of solar wind (vertical grey line). The value in the top right of each panel is the fraction of the distribution that falls in the fast solar wind regime. 81% of quiet and 73% of weak activity occur during slow solar wind. Growth, expansion, driven, and recovery phases occur between 66% and 59% during slow solar wind; recovery bays are equally distributed between fast and slow wind. Multiple intensifications, however, occur 68% during fast solar wind.

The right panels of Fig. 5 show distributions in SYM-H and  $\Lambda$ . An increase in  $\Lambda$  with more negative SYM-H is apparent in many of the distributions, as described by Milan, Hutchinson, et al. (2009) and Milan (2009). A diagonal line,  $\Lambda = 17 - \text{SYM-H}/8$ , has been superimposed to aid discussion. Most distributions peak in the range  $-20 > \text{SYM-H} > 0$  and  $18 < \Lambda < 20^\circ$ , which comprises moderately disturbed conditions. Both quiet and weak activity categories have a significant extension to lower  $\Lambda$ . As  $\Lambda$  increases the trend to more negative SYM-H is clear, especially for driven and recovery phases. The distribution for multiple intensifications appears to be a high- $\Lambda$  extension of the driven phase distribution (in agreement with Milan et al. (2019)). The growth and expansion phase distributions cut off above  $\Lambda \approx 25^\circ$ , whereas the driven and multiple intensifications distributions extend to  $28^\circ$ . The majority of the expansion phase distribution falls above the superimposed diagonal line, the driven phase falls on it, and the recovery phases fall below it: this is consistent with the discussion of Milan, Hutchinson, et al. (2009) regarding the temporal evolution of magnetospheric state during disturbed periods. Finally, we note that the growth phase distribution contains a population with positive SYM-H; as will be discussed in Section 3.2, many growth phases appear to occur at the transition from slow, high-density solar wind (when the magnetopause is compressed) to fast, low-density wind (when dayside driving increases).

### 3.2 Sequence statistics

We now turn to a discussion of the temporal evolution of the system. We can search for particular sequences of categories in our list: for instance, a “classic” isolated sub-storm would comprise the categories quiet then growth, followed by expansion, recovery, and finally quiet (Q-G-E-R-Q). In Figure 6 we perform a superposed epoch analysis of state parameters during the following sequences: (a) Q-W-Q, (b) Q-G-R-Q, (c) Q-G-E-Q, (d) Q-G-E-R-Q, (e) Q-G-E-D-Q, (f) Q-G-E-D-R-Q, (g) Q-G-E-D-RB-Q, where W, D, and RB refer to weak activity, driven phases, and recovery bays. The zero epoch is the end of the initial quiet phase. The time axis is constructed so that the duration of each category is normalised to its average within the ensemble. Only one hour of the preceding and following quiet periods is shown, though in practice these may be longer.

Case (a) represents an interval of weak driving amongst otherwise quiet conditions. This is marked by  $\Phi_D^* \approx \Phi_{PC}^* \approx 7$  kV and  $AU \approx -AL \approx 40$  nT over a period of 3 h.  $\Lambda$  rises from  $16^\circ$  during the quiet periods to  $17^\circ$  during the weak activity.



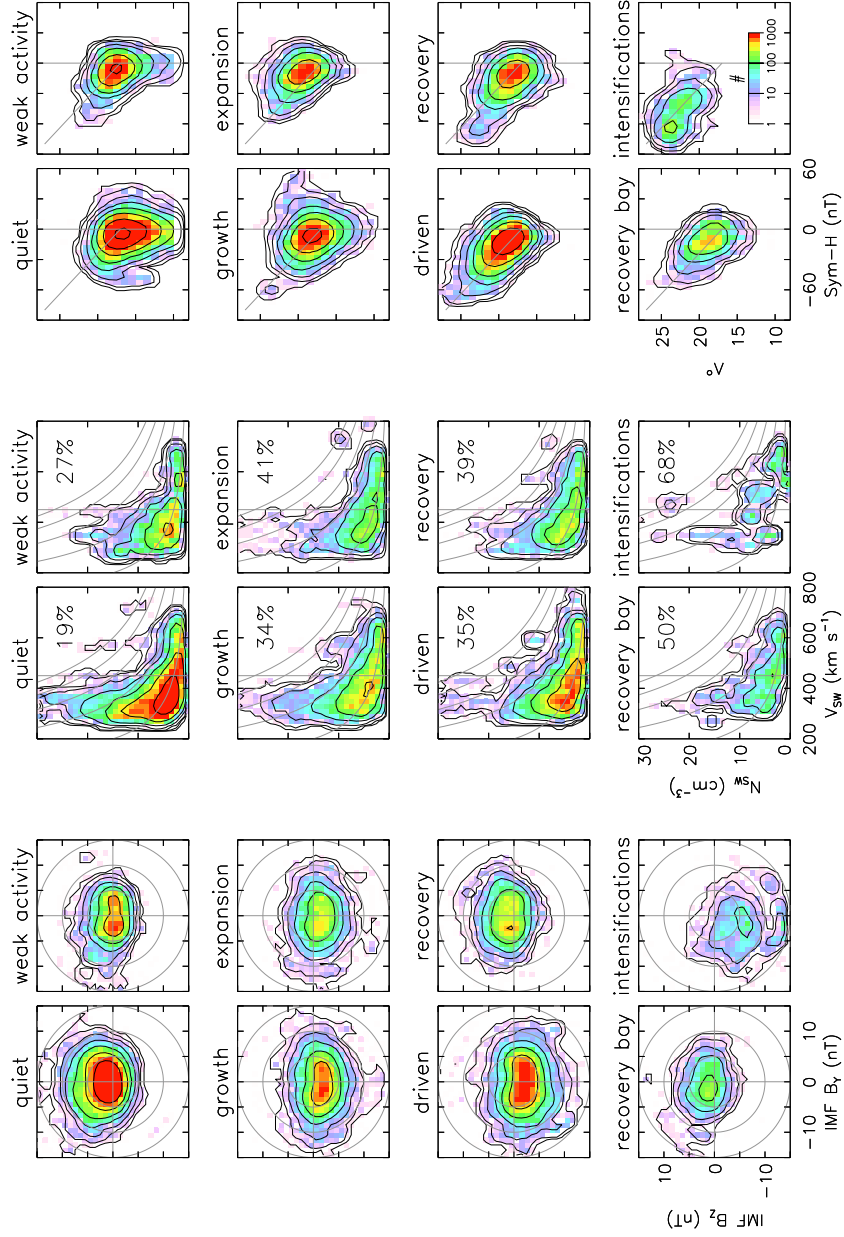


**Figure 5.** (Left) Occurrence distributions of the IMF  $B_y$  and  $B_z$  components during each category, on a log scale. (Middle) Distributions of solar wind speed,  $V_{sw}$ , and density,  $N_{sw}$ . Grey curves show loci of solar wind ram pressure of 1, 3, 5, 7, and 9 nPa. The vertical grey line shows an approximate demarcation between slow and fast solar wind; the fraction of the distribution that is associated with fast solar wind is shown in the top right. (Right) Distributions of SYM-H and FAC radius,  $\Lambda$ . A diagonal grey line,  $\Lambda = 17 - \text{SYM-H}/8$ , is added for reference.



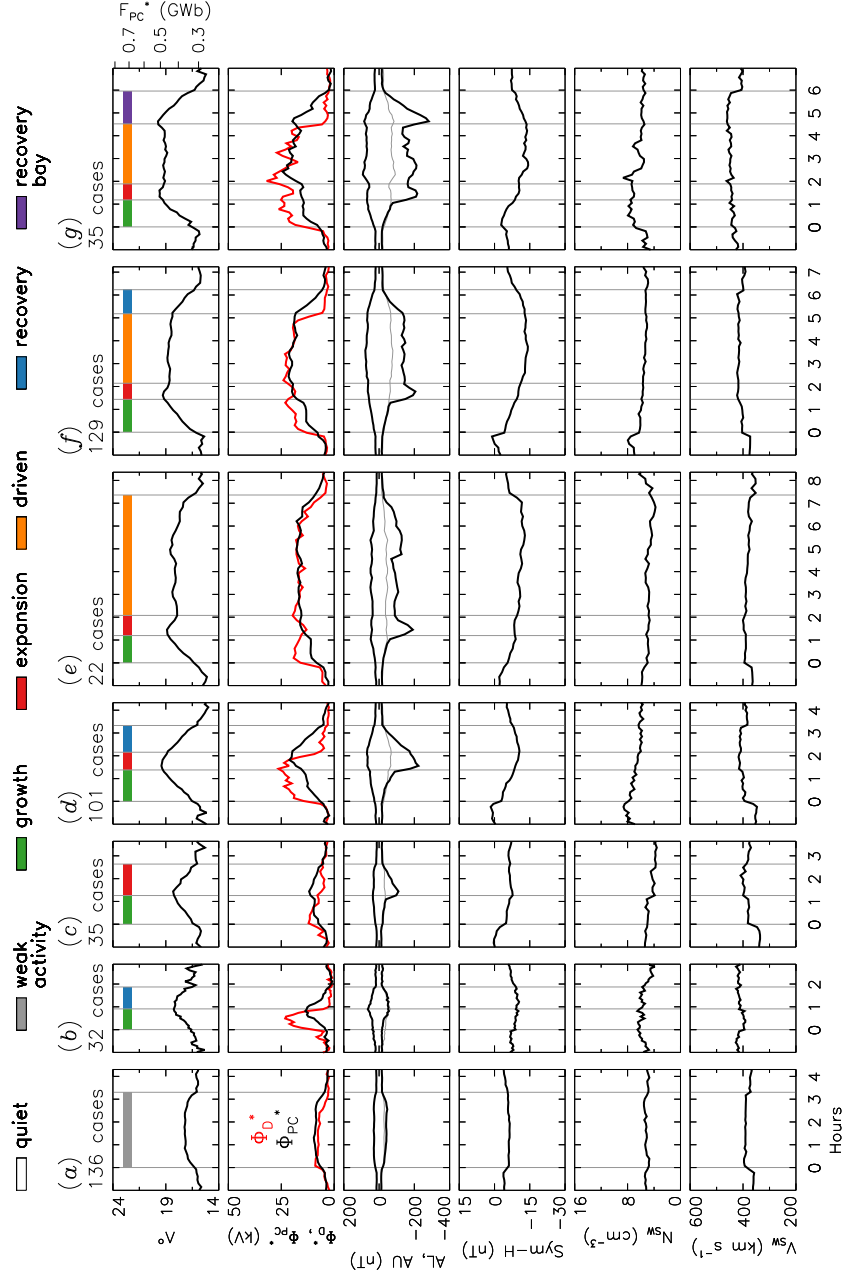


**Figure 6.** Superposed epoch analyses of different sequences of categories (see text for details). In each case the duration of each category has been normalised to the average duration of the ensemble.

Next we discuss case (d), the classic isolated substorm. Reconnection switches on with  $\Phi_D^* \approx 20$  kV, and during the ensuing growth phase lasting just over an hour the polar cap expands to  $\Lambda \approx 20^\circ$ . AL and AU increase in magnitude through this phase, with  $AU \approx -AL$  indicating that the strengths of the eastward and westward electrojets are comparable, and no substorm electrojet is present. Substorm onset then occurs, with a sudden negative excursion of AL to  $-200$  nT, marking the formation of the substorm electrojet. Dayside reconnection is still ongoing at this stage but eventually ceases with a northward turning of the IMF, after 50 mins on average. The magnetosphere enters recovery phase, and the polar cap contracts and AU and AL return to quiet time values over the course of 70 mins. Through this sequence we expect that  $\Phi_D > 0$ ,  $\Phi_N = 0$  during the growth phase,  $\Phi_D > 0$ ,  $\Phi_N > 0$  during the expansion phase, and  $\Phi_D = 0$ ,  $\Phi_N > 0$  during the recovery phase. As discussed in the introduction, we expect  $\Phi_{PC}$  to approximate a smoothed moving average of  $\Phi_D$  and  $\Phi_N$ , and indeed this is the observed behaviour of  $\Phi_{PC}^*$ .

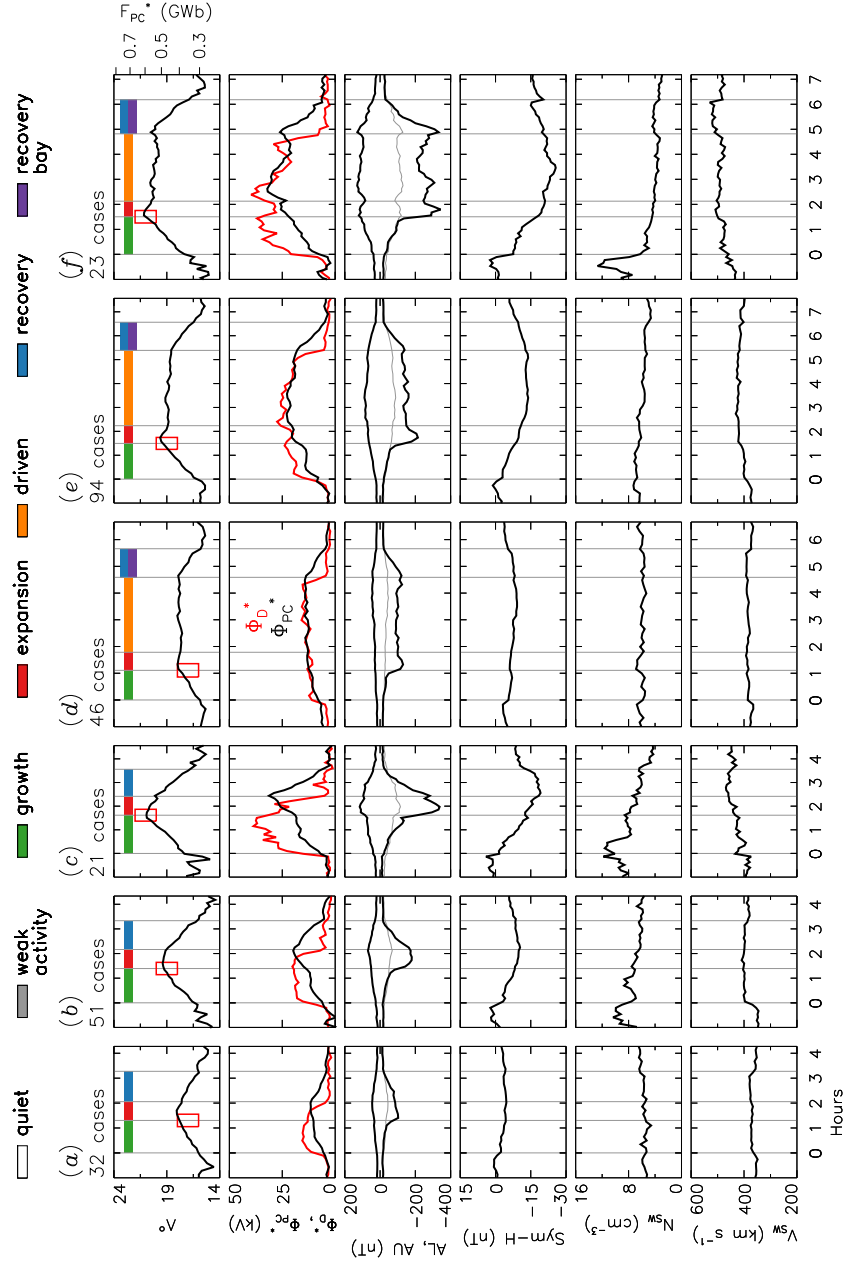
Case (b) represents a period of dayside reconnection,  $\Phi_D^* \approx 20$  kV, during which the polar cap expands to  $\Lambda \approx 18^\circ$ ; however, before a substorm is triggered dayside driving ceases, the magnetosphere enters a recovery phase and the polar cap contracts. AU/AL increase and then decrease, but without the formation of a substorm bay. Case (c) represents a growth phase followed by substorm onset, but in which the dayside driving is weak,  $\Phi_D^* \approx 10$  kV, and decreases following onset such that expansion and recovery phases appear combined.

We now discuss (f), in which dayside driving remains high beyond the point that the substorm bay has begun to diminish. During this driven phase,  $\Phi_N \approx \Phi_D$ ,  $\Lambda$  remains uniform, and the magnitude of AL exceeds that of AU, but not as much as during expansion phase. Eventually, after approximately 3 h on average, dayside driving ceases, but ongoing nightside reconnection leads to a recovery phase during which  $\Lambda$  decreases. Throughout,  $\Phi_{PC}$  is a smoothed moving average of  $\Phi_D$  and  $\Phi_N$ , as expected. Case (g) is similar, but the recovery phase associated with the northward turning of the IMF is accompanied by a significant substorm-like bay. Case (e) is also similar, but rather than an abrupt cessation of dayside driving marking the end of the driven phase,  $\Phi_D$  decreases gradually, as do  $\Phi_N$ ,  $\Phi_{PC}$  and  $\Lambda$ , that is, the driven phase peters out without the occurrence of a clear recovery phase.

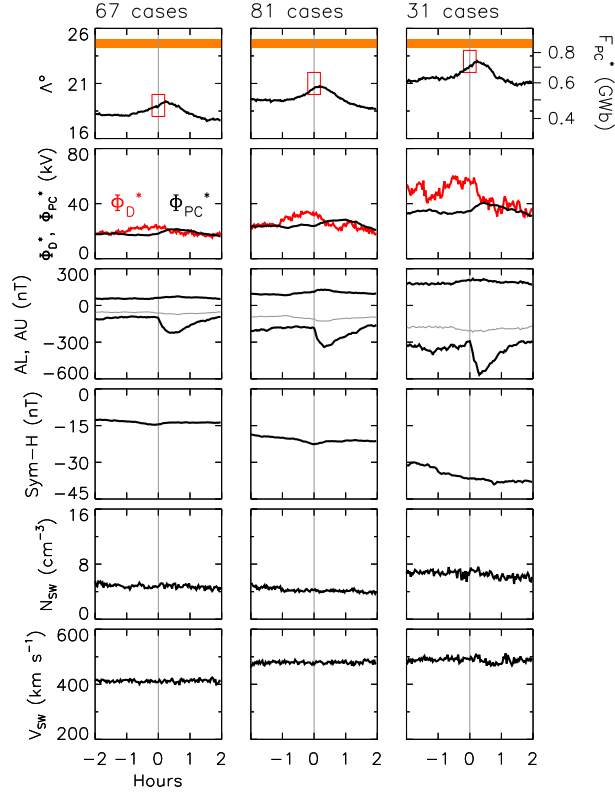
In Figure 7 (a) to (c) we repeat the same analysis for Q-G-E-R-Q sequences (isolated classic substorms), except we subdivide the events by the size of the polar cap at the time of expansion phase onset:  $\Lambda = 16 - 18^\circ$ ,  $18 - 20^\circ$ , and  $20 - 22^\circ$  (indicated by the red boxes in the upper panels). Substorms with greater  $\Lambda$  at onset are driven by larger  $\Phi_D^*$  during the growth phase, have higher  $\Phi_{PC}^*$ , and are more intense as measured in AL, all results consistent with previous findings (Milan, Grocott, et al., 2009; Clausen et al., 2013; Coxon et al., 2014).

Fig. 7 (d) to (f) show the same analysis for Q-G-E-D-R/RB-Q sequences (substorms with a driven phase, and ending in either a recovery phase or recovery bay), again subdivided by  $\Lambda$  at onset. The growth and expansion phases behave similarly to the isolated substorms, which is to be expected as the subsequent activity (driven phase or not) is determined by the behaviour of the IMF after onset. We find that  $\Lambda$  during the driven phase is dependent on the preceding behaviour, that is the polar cap is larger during more strongly driven events.

Examining the behaviour of SYM-H in Fig. 7, we note that it starts near 0 during the quiet period, decreases during the growth and expansion phases (more-so during strongly driven substorms), and plateaus during a subsequent driven phase. It is possible that  $\Lambda$  during the driven phase is controlled by SYM-H, as proposed by Milan, Hutchinson, et al. (2009). For both substorms with and without a driven phase, the more strongly driven cases appear on average to have a step in solar wind density near the start of the



**Figure 7.** Superposed epoch analyses of growth-expansion-recovery and growth-expansion-driven-recovery sequences (see text for details). These are repeated three times for expansion phases that commence for  $16 < \Lambda < 18^\circ$ ,  $18 < \Lambda < 20^\circ$ , and  $20 < \Lambda < 22^\circ$  (indicated by the red boxes).



**Figure 8.** Superposed epoch analyses of driven phase onsets from two hours before to two hours after onset. This is repeated three times for onsets for which  $18 < \Lambda < 20^\circ$ ,  $20 < \Lambda < 22^\circ$ , and  $22 < \Lambda < 24^\circ$  (indicated by the red boxes).

growth phase (also apparent as a simultaneous positive excursion of SYM-H). We also note that more weakly and more strongly driven cases are on average associated with lower ( $350 \text{ km s}^{-1}$ ) and higher ( $500 \text{ km s}^{-1}$ ) solar wind speed, respectively.

In many of the substorms identified in Fig. 3,  $F_{PC}^*$  continues to grow for 20 mins or so after expansion phase onset. This behaviour is also seen in some of the superposed epoch analyses of Fig. 6. On one hand, in most cases  $\Phi_D^*$  remains high after onset, so open flux continues to be accumulated even after nightside reconnection has commenced, and if  $\Phi_D > \Phi_N$  then  $F_{PC}$  will continue to grow. On the other hand, the assumption that the polar cap is circular, used to calculate  $F_{PC}^*$ , is likely to break down at these times due to the formation of a substorm auroral bulge (Mooney et al., 2020), and it is possible that  $F_{PC}^*$  overestimates the true polar cap flux during the expansion phase.

### 3.3 Driven phase onsets

As mentioned in Section 2.2.5, there is an additional category of substorm-like onset that can occur during prolonged driven phases. These driven phase onsets are studied in Figure 8, which presents superposed-epoch analyses from 2 h before to 2 h after these onsets; these have been subdivided by  $\Lambda = 18 - 20^\circ$ ,  $20 - 22^\circ$ , and  $22 - 24^\circ$  at onset (delineated by the red boxes in the upper panels). In total, 196 such events were identified in this study (on average one for every 10 h of driven phase duration over the course of the year).

Driven phases are periods of quasi-balanced dayside and nightside reconnection,  $\Phi_N \approx \Phi_D$  and  $F_{PC} \approx \text{const}$ , that is, periods during which the magnetotail has adjusted itself to release magnetic flux at the same rate that it is being accumulated on the dayside. However,  $\Phi_D$  responds promptly to changes in the solar wind, whereas  $\Phi_N$  appears to respond more slowly. For instance, an abrupt northwards turning of the IMF can lead to a sudden decrease in  $\Phi_D$  but nightside reconnection can continue unabated, resulting in a decrease in  $F_{PC}$  (which we define as a recovery phase).

Driven phase onsets appear to be the response to more gradual changes in  $\Phi_D$ , specifically moderate increases. Fig. 8 shows that on average 2 h prior to each onset  $\Phi_D^* \approx \Phi_{PC}^*$ , but that a slight increase in  $\Phi_D^*$  occurs approximately 1 h before.  $\Phi_{PC}^*$  remains unchanged at this time, suggesting that  $\Phi_N$  also continues uniformly. Dayside and nightside reconnection are now slightly unbalanced leading to an increase in  $F_{PC}$  ( $\Lambda$ ). Eventually this situation can no longer be supported and onset occurs:  $\Lambda$  decreases and  $\Phi_{PC}^*$  increases, accompanied by a bay in AL, all lasting approximately 90 mins. These observations suggest that  $\Phi_N$  has suddenly increased to exceed  $\Phi_D$  for the duration of these 90 min, accompanied by the formation of a substorm current wedge, presumably associated with a new NENL.

After 90 mins,  $\Phi_D$  and  $\Phi_N$  are balanced once again. Indeed, the increase in  $\Phi_D^*$  that triggers the onset is reversed shortly after onset, on average. We interpret this as being due to the natural short-term variability of the IMF, coupled with the fact that enhanced  $\Phi_D$  is no longer necessary to trigger a driven phase onset. This is essentially the same argument put forward by Freeman and Morley (2004) for explaining the apparent association between substorm onsets and northwards turnings of the IMF in superposed epoch analyses (e.g., Caan et al., 1977; Lyons, 1995).

We have argued that classic substorms are those that occur within an hour or so of a southward turning of the IMF, and for which the IMF turns northwards again shortly after onset. The expansion phase of these substorms marks the establishment of a NENL and the formation of a substorm current wedge, which produces a bay in AL, in response to the accumulation of open magnetic flux in the magnetotail. If the IMF remains southwards for a significant period, the magnetosphere can segue from substorm expansion phase to what we have termed the driven phase, when dayside and nightside reconnection are balanced. Within these driven phases, modest increases in the dayside reconnection rate can result in a further accumulation of open flux in the magnetotail, leading to a driven phase onset, again accompanied by a bay in AL. Our interpretation is that during driven phases the NENL has evolved into a DNL. Subsequent increases in magnetotail flux may trigger the formation of a new NENL and SCW, leading to the driven phase onset bay. Hence, we identify driven phase onsets and classic substorms with intervals of NENL formation when a DNL is active or absent down-tail, respectively. The near-Earth tail dynamics that occur during these two types of event are essentially the same, but occur within the context of differing magnetospheric convection, and subsequently contribute towards that convection. Hence, what are referred to as the “directly-driven” and “loading-unloading” aspects of magnetospheric activity – or the “two-component auroral electrojets” (Kamide & Kokubun, 1996) – are two sides of the same coin.

Finally, we note that the higher  $\Lambda$  cases occur during periods of higher magnitude SYM-H, again consistent with the suggestion that ring current intensity modulates the stability of the magnetotail to the onset of reconnection in the near-Earth tail (Milan, Hutchinson, et al., 2009). In addition, higher  $\Lambda$  cases are associated with higher solar wind speeds.

Besides the onsets described above, there are often substorm-like bays in AL during driven phases that do not appear associated with changes in solar wind conditions or significant variations in  $F_{PC}$ . DeJong (2014) also noted the variability of AL during strongly driven SMC periods, and Milan et al. (2006) reported multiple tail dipolarisa-

tions during a substorm prolonged by ongoing dayside reconnection. These fluctuations are most intense during periods of multiple intensifications, which are associated with the largest values of  $\Lambda$ . It is unclear what these fluctuations represent – a rapidly reforming NENL, repeated intensifications of an active NENL, or some other explanation – and this requires further study.

### 3.4 Relation to solar wind structure and variability

In section 3.1 we investigated the solar wind conditions during different convection categories. The differences between the  $N_{SW}-V_{SW}$  distributions was not great, though quiet periods were predominantly found during slow solar wind conditions. This can be understood through the  $V_{SW}$  contribution to  $\Phi_D^*$  in eq. (5): slow solar wind in general leads to low  $\Phi_D^*$  unless a solar wind structure leads to unusually high IMF magnitude.

2010 comprised repeating periods of fast solar wind with low density followed by slow solar wind with highly variable density. Figure 9 shows two such intervals, comprising days-of-year (DOYs) 164 to 194 and 281 to 311. The upper panel shows the fraction of each day occupied by different states; the next panel shows the open flux accumulated by dayside reconnection during each day, broken down by category. Below this are the times of onsets of expansion phases (red ticks) and driven phase onsets (blue ticks),  $\Lambda^\circ$ , IMF  $B_Z$ ,  $V_{SW}$  and  $N_{SW}$ , AU and AL, and SYM-H. We note the anti-correlation between SYM-H and  $\Lambda$ , previously reported by Milan, Hutchinson, et al. (2009).

Prolonged quiet periods are associated with slow solar wind (DOY 170-172, 186-188, 287, 303-305) and/or extended IMF  $B_Z > 0$  (DOY 172, 304-305). Conversely, periods of high flux transport can be associated with fast solar wind (DOY 167, 180-184, 296-297). Some periods of high  $\Phi_D^*$  occur after steps in solar wind density, when the solar wind may be slow but the IMF is compressed and has a relatively high magnitude (DOY 190, 284-285); such periods contribute to the high solar wind density seen at the start of growth phases as discussed in relation to Figs. 6 and 7. Other periods have moderately high solar wind speed but low  $\Phi_D^*$  (DOY 300-301) because the  $B_Z$  component of the IMF is of low magnitude.

In addition, although the general solar wind conditions may be similar during two different periods, the nature of the coupling can vary: for instance, compare DOY 180-184, when most flux transport occurs during driven phases, with DOY 295-299, when expansion phases dominate. In the latter case the  $B_Z$  component of the IMF oscillated north-south with a period of a few hours, leading to multiple isolated substorms, whereas  $B_Z < 0$  was more sustained during the former period.

We conclude that the detailed nature of convection is determined by the details of relatively short-lived variations in the solar wind and IMF, within an overarching expectation that prolonged periods of high and low solar wind speed tend to lead to stronger and weaker convection.

## 4 Conclusions

Using proxies for the dayside reconnection rate,  $\Phi_D^*$ , cross-polar cap potential,  $\Phi_{PC}^*$ , open magnetic flux,  $F_{PC}^*$ , and the electrojet indices, AU and AL, we have identified convection state continuously throughout 2010. The states we identify are: quiet (which occurs 46% of the time and accounts for 13% of the magnetic flux throughput of the magnetosphere), weak activity (9%, 6%), the substorm phases of growth (11%, 21%), expansion (5%, 10%), driven (18%, 38%), and recovery (8%, 5%), and storm periods comprising multiple intensifications (1%, 8%).

The driven phase occurs after substorm expansion phase if the IMF remains southwards for a prolonged period, and ends with the subsequent northward turning. This rep-

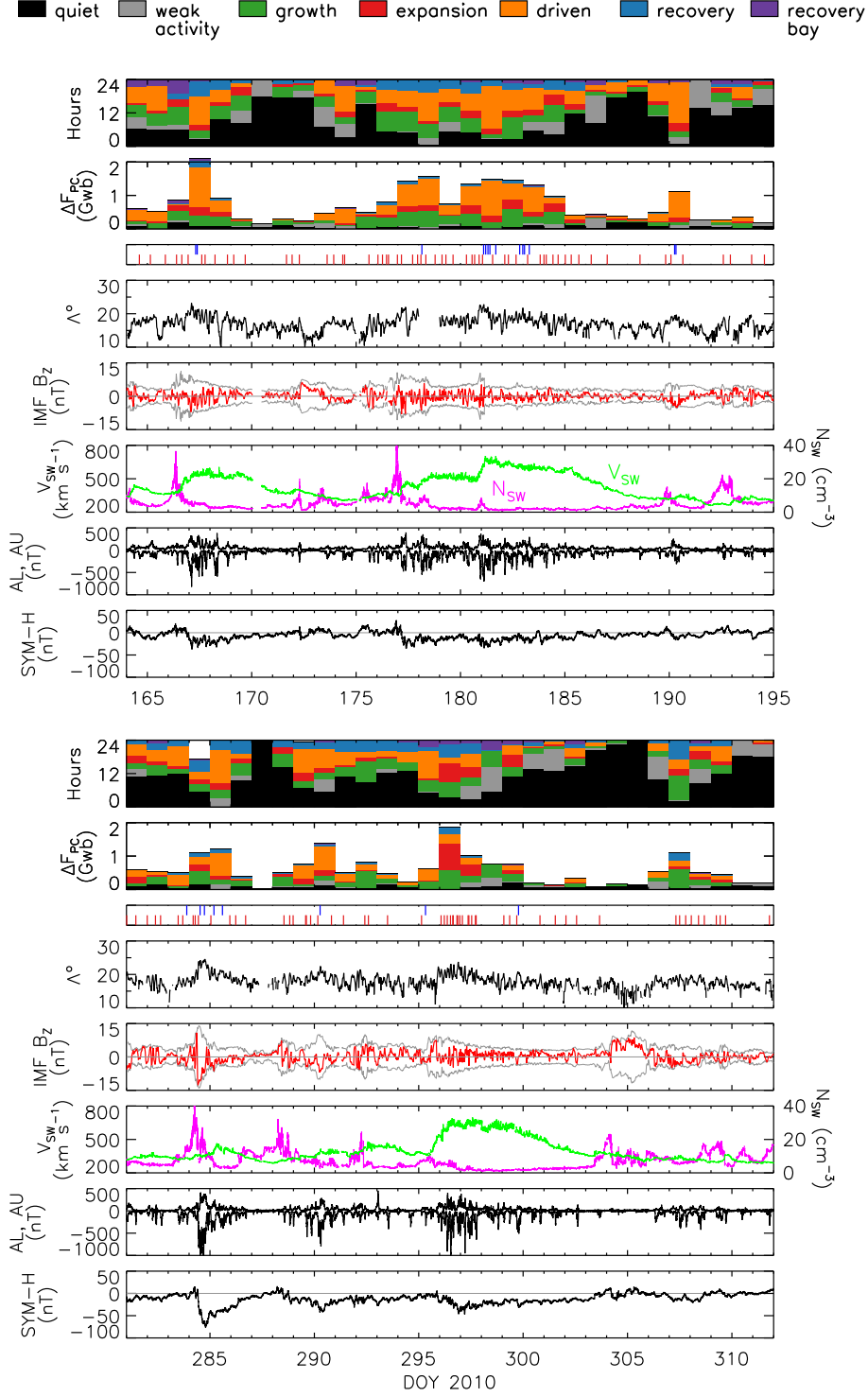


**Figure 9.** A comparison of two 31-day periods from 2010, showing broadly similar solar wind speed and density structures. The upper two panels show the fraction of each day occupied by different convection categories and the amount of open flux accumulated by dayside reconnection during each category ( $\Delta F_{PC}$ ). Red and blue ticks show the times of expansion phase onsets (red) and driven phase onsets (blue). In the IMF  $B_z$  panel, the grey curves show the envelope of the total IMF magnitude.



resents intervals when the nightside reconnection rate is quasi-balanced with the day-side rate such that the magnetosphere enters a state of steady convection. Following a cessation of dayside driving, the nightside rate remains elevated for an hour or so, leading to the recovery phase. During these driven phases, modest variations of  $\Phi_D$  can lead to slight imbalances with  $\Phi_N$  which result in gradual variations in  $F_{PC}$ . In the case of  $\Phi_D > \Phi_N$ , a gradual increase in  $F_{PC}$  can lead to a new substorm onset, signalled by an AL bay and an abrupt enhancement in  $\Phi_N$  leading to a decrease in  $F_{PC}$ ; thereafter, the driven phase can continue. We refer to these as driven phase onsets.

Besides driven phase onsets, there can be significant bay-like activity in AL during driven phases, but without attendant variations in  $F_{PC}$ . The cause of these bays is not yet understood, but they could be reformations of the NENL or re-intensifications of already ongoing tail reconnection. Further work is necessary to identify the nature of these onsets.

In our scheme, we identify growth phases as periods of dayside but no nightside reconnection, expansion phases as the onset of nightside reconnection at a near-Earth neutral line, we assume driven phases occur once the NENL has progressed down-tail to form a distant neutral line, and recovery phases as ongoing DNL reconnection after dayside reconnection has ceased. We interpret driven phase onsets as the formation of a new NENL whilst a DNL is already active. This provides a framework for understanding the difference between isolated substorms and those occurring during ongoing activity. Isolated substorms are associated with brief southward turnings of the IMF. Longer periods of driving result in substorm driven phases, during which driven phase onsets can occur. This framework encompasses the two-component auroral electrojet model of Kamide and Kokubun (1996).

The size of the polar cap is strongly influenced by SYM-H. As speculated in previous studies (e.g., Milan, Hutchinson, et al., 2009; Milan, 2009), we suggest that the criterion for reconnection onset in the tail is a balance between two competing factors: thinning of the plasma sheet by the pressure produced by inflated lobes (hence a growth phase being required prior to onset), and the magnetic perturbation introduced by the ring current into the magnetotail which counteracts the thinning. The magnitude of SYM-H then controls the value of  $F_{PC}$  required for substorm onset and the equilibrium level of  $F_{PC}$  during driven phases. Fig. 7 indicates that SYM-H grows during the growth phase at a rate that is controlled by  $\Phi_D$ . This in turn dictates the size of the polar cap at the time of substorm onset. SYM-H and  $F_{PC}$  plateau during any subsequent driven phase. SYM-H then controls the level of  $F_{PC}$  required for driven phase onsets to occur.

Approximately a quarter of recovery phases are associated with a bay in AL, which we refer to as recovery bays. The nature and cause of these recovery bays is not yet clear and will be investigated in future work, including a comparison with the bays associated with substorm onsets, driven phase onsets, and other bay-like activity in AL.

In this study we have analysed magnetospheric state for the duration of the year 2010, the beginning of solar cycle 24. Due to the relative complexity of the task, the classification was done by hand (a somewhat labourious undertaking). However, AMPERE data is currently available for the period 2010 to 2016, encompassing the rising phase and maximum of the solar cycle, providing a means to study in detail the long-term influence of solar activity on magnetospheric convection. We hope to use the dataset we have produced so far to develop an automated procedure to extend the classification to the whole seven-year interval.

## Acknowledgments

SEM and JAC were supported by the Science and Technology Facilities Council (STFC), UK, grant no. ST/S000429/1; HS and GB were supported by STFC studentships. The

work at the Birkeland Centre for Space Centre, University of Bergen, Norway, was supported by the Research Council of Norway/CoE under contract 223252/F50. We thank the AMPERE team and the AMPERE Science Center for providing the Iridium-derived data products; AMPERE products are available at <http://ampere.jhuapl.edu>. The AMPERE FAC radii dataset is available at <https://doi.org/10.25392/leicester.data.11294861.v1>. The convection state data accompanying this paper is available at <https://doi.org/10.25392/leicester.data.12571307.v1>. The OMNI data, including solar wind parameters and geomagnetic indices, were obtained from the GSFC/SPDF OMNIWeb interface at <http://omniweb.gsfc.nasa.gov>.

## References

- Anderson, B., Takahashi, K., Kamei, T., Waters, C., & Toth, B. (2002). Birkeland current system key parameters derived from Iridium observations: Method and initial validation results. *Journal of Geophysical Research: Space Physics*, 107(A6), SMP–11.
- Anderson, B., Takahashi, K., & Toth, B. (2000). Sensing global Birkeland currents with Iridium® engineering magnetometer data. *Geophysical Research Letters*, 27(24), 4045–4048.
- Baker, D. N., Pulkkinen, T., Angelopoulos, V., Baumjohann, W., & McPherron, R. (1996). Neutral line model of substorms: Past results and present view. *Journal of Geophysical Research: Space Physics*, 101(A6), 12975–13010.
- Boakes, P., Milan, S., Abel, G., Freeman, M., Chisham, G., Hubert, B., & Sotirelis, T. (2008). On the use of image fuv for estimating the latitude of the open/closed magnetic field line boundary in the ionosphere. In *Annales geophysicae* (Vol. 26, pp. 2759–2769).
- Burrell, A., Chisham, G., Milan, S., Kilcommons, L., Chen, Y.-J., Thomas, E., & Anderson, B. (2020). Ampere polar cap boundaries. In *Annales geophysicae* (Vol. 38, pp. 481–490).
- Caan, M. N., McPherron, R. L., & Russell, C. T. (1977). Characteristics of the association between the interplanetary magnetic field and substorms. *Journal of Geophysical Research*, 82(29), 4837–4842.
- Clausen, L., Baker, J., Ruohoniemi, J., Milan, S., & Anderson, B. (2012). Dynamics of the region 1 Birkeland current oval derived from the Active Magnetosphere and Planetary Electrodynamics Response Experiment (AMPERE). *Journal of Geophysical Research: Space Physics*, 117(A6).
- Clausen, L., Milan, S., Baker, J., Ruohoniemi, J., Glassmeier, K.-H., Coxon, J., & Anderson, B. (2013). On the influence of open magnetic flux on substorm intensity: Ground-and space-based observations. *Journal of Geophysical Research: Space Physics*, 118(6), 2958–2969.
- Cowley, S., & Lockwood, M. (1992). Excitation and decay of solar wind-driven flows in the magnetosphere-ionosphere system. In *Annales geophysicae* (Vol. 10, pp. 103–115).
- Coxon, J., Milan, S., & Anderson, B. (2018). A review of Birkeland current research using AMPERE. *Electric currents in geospace and beyond*, 257–278.
- Coxon, J., Milan, S., Clausen, L., Anderson, B., & Korth, H. (2014). A superposed epoch analysis of the regions 1 and 2 Birkeland currents observed by AMPERE during substorms. *Journal of Geophysical Research: Space Physics*, 119(12), 9834–9846.
- Davis, T. N., & Sugiura, M. (1966). Auroral electrojet activity index AE and its universal time variations. *Journal of Geophysical Research*, 71(3), 785–801.
- DeJong, A. (2014). Steady magnetospheric convection events: How much does steadiness matter? *Journal of Geophysical Research: Space Physics*, 119(6), 4389–4399.

- DeJong, A., Ridley, A., & Clauer, C. (2008). Balanced reconnection intervals: Four case studies. *Annales Geophysicae*.
- Dungey, J. W. (1961). Interplanetary magnetic field and the auroral zones. *Physical Review Letters*, 6(2), 47.
- Forsyth, C., Rae, I., Coxon, J., Freeman, M., Jackman, C., Gjerloev, J., & Fazakerley, A. (2015). A new technique for determining Substorm Onsets and Phases from Indices of the Electrojet (SOPHIE). *Journal of Geophysical Research: Space Physics*, 120(12), 10–592.
- Freeman, M., & Morley, S. (2004). A minimal substorm model that explains the observed statistical distribution of times between substorms. *Geophysical research letters*, 31(12).
- Frey, H., Mende, S., Angelopoulos, V., & Donovan, E. (2004). Substorm onset observations by IMAGE-FUV. *Journal of Geophysical Research: Space Physics*, 109(A10).
- Hones Jr., E. (1984). Plasma sheet behavior during substorms. In E. W. H. Jr. (Ed.), *Magnetic Reconnection in Space and Laboratory Plasmas* (Vol. 30, pp. 178–184). Washington, D.C.: AGU.
- Hubert, B., Gérard, J.-C., Milan, S. E., & Cowley, S. W. (2017). Magnetic reconnection during steady magnetospheric convection and other magnetospheric modes. In *Annales geophysicae* (Vol. 35, pp. 505–524).
- Hubert, B., Milan, S., Grocott, A., Blockx, C., Cowley, S., & Gérard, J.-C. (2006). Dayside and nightside reconnection rates inferred from IMAGE FUV and Super Dual Auroral Radar Network data. *Journal of Geophysical Research: Space Physics*, 111(A3).
- Iijima, T., & Potemra, T. (1976). The amplitude distribution of field-aligned currents at northern high latitudes observed by Triad. *Journal of Geophysical Research*, 81(13), 2165–2174.
- Iijima, T., & Potemra, T. (1978). Large-scale characteristics of field-aligned currents associated with substorms. *Journal of Geophysical Research: Space Physics*, 83(A2), 599–615.
- Iyemori, T. (1990). Storm-time magnetospheric currents inferred from mid-latitude geomagnetic field variations. *Journal of geomagnetism and geoelectricity*, 42(11), 1249–1265.
- Kamide, Y., & Kokubun, S. (1996). Two-component auroral electrojet: Importance for substorm studies. *Journal of Geophysical Research: Space Physics*, 101(A6), 13027–13046.
- Kan, J., & Lee, L. (1979). Energy coupling function and solar wind-magnetosphere dynamo. *Geophysical Research Letters*, 6(7), 577–580.
- King, J., & Papitashvili, N. (2005). Solar wind spatial scales in and comparisons of hourly Wind and ACE plasma and magnetic field data. *Journal of Geophysical Research: Space Physics*, 110(A2).
- Kissinger, J., McPherron, R., Hsu, T.-S., & Angelopoulos, V. (2011). Steady magnetospheric convection and stream interfaces: Relationship over a solar cycle. *Journal of Geophysical Research: Space Physics*, 116(A5).
- Kissinger, J., McPherron, R., Hsu, T.-S., Angelopoulos, V., & Chu, X. (2012). Necessity of substorm expansions in the initiation of steady magnetospheric convection. *Geophysical research letters*, 39(15).
- Lockwood, M. (1991). On flow reversal boundaries and transpolar voltage in average models of high-latitude convection. *Planetary and space science*, 39(3), 397–409.
- Lockwood, M., & Cowley, S. (1992). Ionospheric convection and the substorm cycle. *Proceedings of the International Conference on Substorms (ICS-1)*, 99–109.
- Lockwood, M., Hairston, M., Finch, I., & Rouillard, A. (2009). Transpolar voltage and polar cap flux during the substorm cycle and steady convection events. *Journal of Geophysical Research: Space Physics*, 114(A1).

- Lyons, L. (1995). A new theory for magnetospheric substorms. *Journal of Geophysical Research: Space Physics*, 100(A10), 19069–19081.
- McPherron, R. L. (1970). Growth phase of magnetospheric substorms. *Journal of Geophysical Research*, 75(28), 5592–5599.
- McPherron, R. L., Russell, C. T., & Aubry, M. P. (1973). Satellite studies of magnetospheric substorms on August 15, 1968: 9. Phenomenological model for substorms. *Journal of Geophysical Research*, 78(16), 3131–3149.
- McWilliams, K., Pfeifer, J., & McPherron, R. (2008). Steady magnetospheric convection selection criteria: Implications of global superdarn convection measurements. *Geophysical research letters*, 35(9).
- Milan, S. (2004). Dayside and nightside contributions to the cross polar cap potential: placing an upper limit on a viscous-like interaction. *Annales Geophysicae*, 22, 3771–3777.
- Milan, S. (2009). Both solar wind-magnetosphere coupling and ring current intensity control of the size of the auroral oval. *Geophysical Research Letters*, 36(18).
- Milan, S. (2013). Modeling birkeland currents in the expanding/contracting polar cap paradigm. *Journal of Geophysical Research: Space Physics*, 118(9), 5532–5542.
- Milan, S. (2015). Sun et lumière: Solar wind-magnetosphere coupling as deduced from ionospheric flows and polar auroras. In *Magnetospheric Plasma Physics: The Impact of Jim Dungey's Research* (pp. 33–64). Springer.
- Milan, S. (2019). *AMPERE R1/R2 FAC radii. figshare. Dataset*. <https://doi.org/10.25392/leicester.data.11294861.v1>. doi: 10.25392/leicester.data.11294861.v1
- Milan, S. (2020). *Magnetospheric Geonome Project 2010. University of Leicester. Dataset*. <https://doi.org/10.25392/leicester.data.12571307.v1>. doi: 10.25392/leicester.data.12571307.v1
- Milan, S., Boakes, P., & Hubert, B. (2008). Response of the expanding/contracting polar cap to weak and strong solar wind driving: Implications for substorm onset. *Journal of Geophysical Research: Space Physics*, 113(A9).
- Milan, S., Carter, J., Korth, H., & Anderson, B. (2015). Principal component analysis of birkeland currents determined by the active magnetosphere and planetary electrodynamics response experiment. *Journal of Geophysical Research: Space Physics*, 120(12), 10–415.
- Milan, S., Clausen, L., Coxon, J., Carter, J., Walach, M.-T., Laundal, K., ... others (2017). Overview of solar wind-magnetosphere-ionosphere-atmosphere coupling and the generation of magnetospheric currents. *Space Science Reviews*, 206(1-4), 547–573.
- Milan, S., Gosling, J., & Hubert, B. (2012). Relationship between interplanetary parameters and the magnetopause reconnection rate quantified from observations of the expanding polar cap. *Journal of Geophysical Research: Space Physics*, 117(A3).
- Milan, S., Grocott, A., Forsyth, C., Imber, S., Boakes, P. D., & Hubert, B. (2009). A superposed epoch analysis of auroral evolution during substorm growth, onset and recovery: Open magnetic flux control of substorm intensity. *Annales Geophysicae*, 27(2), 659–668.
- Milan, S., Hutchinson, J., Boakes, P., & Hubert, B. (2009). Influences on the radius of the auroral oval. *Annales Geophysicae*, 27(7), 2913–2924.
- Milan, S., Lester, M., Cowley, S., Oksavik, K., Brittnacher, M., Greenwald, R., ... Villain, J.-P. (2003). Variations in the polar cap area during two substorm cycles. *Annales Geophysicae*, 21(5), 1121–1140.
- Milan, S., Provan, G., & Hubert, B. (2007). Magnetic flux transport in the Dungey cycle: A survey of dayside and nightside reconnection rates. *Journal of Geophysical Research: Space Physics*, 112(A1).
- Milan, S., Walach, M.-T., Carter, J., Sangha, H., & Anderson, B. (2019). Sub-

- storm onset latitude and the steadiness of magnetospheric convection. *Journal of Geophysical Research: Space Physics*, 124(3), 1738–1752.
- Milan, S., Wild, J., Hubert, B., Carr, C. M., Lucek, E., Bosqued, J., ... Slavin, J. (2006). Flux closure during a substorm observed by Cluster, Double Star, IMAGE FUV, SuperDARN, and Greenland magnetometers. In *Annales geophysicae* (Vol. 24, pp. 751–767).
- Mooney, M., Forsyth, C., Rae, I., Chisham, G., Coxon, J., Marsh, M., ... Hubert, B. (2020). Examining local time variations in the gains and losses of open magnetic flux during substorms. *Journal of Geophysical Research: Space Physics*.
- Newell, P., & Gjerloev, J. (2011). Evaluation of SuperMAG auroral electrojet indices as indicators of substorms and auroral power. *Journal of Geophysical Research: Space Physics*, 116(A12).
- Rostoker, G., Akasofu, S.-I., Foster, J., Greenwald, R., Kamide, Y., Kawasaki, K., ... Russell, C. (1980). Magnetospheric substorms—definition and signatures. *Journal of Geophysical Research: Space Physics*, 85(A4), 1663–1668.
- Russell, C. (2000). How northward turnings of the IMF can lead to substorm expansion onsets. *Geophysical research letters*, 27(20), 3257–3259.
- Sergeev, V., Kubyshkina, M., Liou, K., Newell, P., Parks, G., Nakamura, R., & Mukai, T. (2001). Substorm and convection bay compared: Auroral and magnetotail dynamics during convection bay. *Journal of Geophysical Research: Space Physics*, 106(A9), 18843–18855.
- Sergeev, V., Pellinen, R. J., & Pulkkinen, T. (1996). Steady magnetospheric convection: A review of recent results. *Space Science Reviews*, 75(3-4), 551–604.
- Siscoe, G., & Huang, T. (1985). Polar cap inflation and deflation. *Journal of Geophysical Research: Space Physics*, 90(A1), 543–547.
- Slavin, J., Fairfield, D., Lepping, R., Hesse, M., Ieda, A., Tanskanen, E., ... others (2002). Simultaneous observations of earthward flow bursts and plasmoid ejection during magnetospheric substorms. *Journal of Geophysical Research: Space Physics*, 107(A7), SMP–13.
- Troshichev, O., Dmitrieva, N., & Kuznetsov, B. (1979). Polar cap magnetic activity as a signature of substorm development. *Planetary and space science*, 27(3), 217–221.
- Troshichev, O., Janzhura, A., & Stauning, P. (2006). Unified PCN and PCS indices: Method of calculation, physical sense, and dependence on the IMF azimuthal and northward components. *Journal of Geophysical Research: Space Physics*, 111(A5).
- Walach, M.-T., & Milan, S. (2015). Are steady magnetospheric convection events prolonged substorms? *Journal of Geophysical Research: Space Physics*, 120(3), 1751–1758.
- Waters, C., Anderson, B., & Liou, K. (2001). Estimation of global field aligned currents using the Iridium® system magnetometer data. *Geophysical Research Letters*, 28(11), 2165–2168.